Electric-field tuning of the magnetic properties of bilayer VI₃: A first-principles study

Thi Phuong Thao Nguyen ●, Kunihiko Yamauchi ●,[*] and Tamio Oguchi ●
Institute of Scientific and Industrial Research, Osaka University, 8-1 Mihogaoka, Ibaraki, Osaka 567-0047, Japan

Danila Amoroso ● and Silvia Picozzi
Consiglio Nazionale delle Ricerche (CNR-SPIN), Unità di Ricerca presso Terzi c/o Università "G. D'Annunzio", 66100 Chieti, Italy

The magnetic properties of the two-dimensional VI₃ bilayer are the focus of our first-principles analysis, highlighting the role of t_{2g} orbital splitting and carried out in comparison with the CrI₃ prototypical case, where the splitting is negligible. In VI₃ bilayers, the empty a_{1g} state is found to play a crucial role in both stabilizing the insulating state and in determining the interlayer magnetic interaction. Indeed, an analysis based on maximally localized Wannier functions allows one to evaluate the interlayer exchange interactions in two different VI₃ stackings (labeled AB and AB′), to interpret the results in terms of the virtual-hopping mechanism, and to highlight the strongest hopping channels underlying the magnetic interlayer coupling. Upon application of electric fields perpendicular to the slab, we find that the magnetic ground state in the AB′ stacking can be switched from antiferromagnetic to ferromagnetic, suggesting the VI₃ bilayer as an appealing candidate for electric-field-driven miniaturized spintronic devices.

I. INTRODUCTION

Boosted by the experimental discovery of intrinsic magnetism in atomically thin layers of CrI₃, Cr₂Ge₂Te₆, and Fe₃GeTe₂ [1–3], two-dimensional (2D) van der Waals (vdW) magnets have recently received increasing attention. Interestingly, the control of 2D magnetism in few atomic layers is enabled by external electric field [4–6] or by electron-hole doping [3,7], making them particularly appealing for potential spintronic applications.

Among those materials, VI₃, belonging to the family of transition-metal (M) trihalides MX₃ (X = Cl, B, and I) with honeycomb arrangement of the metal cations (similar to the most studied CrI₃ [1,4–13]), has recently emerged as a potential 2D ferromagnet [14–20]. It is known since more than 30 years ago that, in the bulk form, VI₃ becomes ferromagnetic below a Curie temperature of $T_c \simeq 55$ K, similar to CrI₃ (with $T_c \simeq 68$ K) [21]. Conversely, the structural properties are still under debate. Experimental characterizations of the crystal structure have in fact reported that VI₃ undergoes a structural phase transition around 79 K, changing its symmetry across still unclear phases: The high-temperature crystal structure was proposed to be either trigonal $P31c$ [14] or rhombohedral $R3$ [20], or monoclinic $C2/m$ structure [15]; the low-temperature crystal structure was proposed to be either $C2/c$ [14] or $R\bar{3}$ structure [15]. Optical and electrical transport measurements have clearly showed bulk VI₃ to be a semiconductor with an optical band gap of ∼0.67 eV [14]. However, from the theoretical point of view, the understanding

and modeling of the electronic properties are the focus of the present debate. Some studies have in fact reported that bulk VI₃ is a Mott insulator with a bandgap of about 1 eV [14,15], whereas others have claimed a half-metallic character [19,20].

In a thin-film limit, to the best of our knowledge, no experimental studies have been reported for atomic layers of VI₃. On the theoretical side, current studies are controversial with respect to the electronic properties, in analogy to the situation for the corresponding bulk phase. In particular, by analyzing electronic properties in the VI₃ monolayer, in Ref. [16] a Mott-insulator ground state is proposed, reported to be lower in energy than the half-metallic state (by ∼0.3 eV/f.u.). Other attempts to explain the Mott-insulator ground state have also been reported: The authors in Ref. [17] have proposed orbital-ordered phases accompanying the lattice distortion, while the authors of Ref. [18] ascribed the gap opening to combined effects of spin-orbit coupling (SOC) and Hubbard U correlations. On the other hand, a consensus is reached with respect to the magnetic properties of a VI₃ single layer: Current theoretical characterizations report a ferromagnetic (FM) exchange coupling between first V-site neighbors, i.e., FM intralayer coupling. The interlayer magnetic stability has also been investigated for bilayer VI₃. In particular in Ref. [16] it is reported that the interlayer magnetic stability is sensitive to the layer stacking, in line with previous works on bilayer CrI₃ [9–11]. For the sake of completeness, we mention that in Ref. [22] it is claimed bilayer VI₃ shows a stacking-independent ferromagnetic ground state, but considering the half-metallic state rather than the Mott-insulating one.

A deep understanding of the VI₃ electronic structure is needed to interpret the related magnetic properties, both in the monolayer and in the bilayer case. In this study, we therefore focus on the crucial role of the nondegenerate t_{2g} orbital state in determining the VI₃ insulating behavior and the related

————————
[*]Current address: Elements Strategy Initiative for Catalysts and Batteries (ESICB), Kyoto University, Kyoto 615-8245, Japan; kunihiko@sanken.osaka-u.ac.jp

magnetic properties. As a counterexample, we consider the prototypical 2D magnet CrI$_3$ (where t_{2g} orbitals are almost degenerate), and we carry out a one-to-one comparison between VI$_3$ and CrI$_3$. In particular, we first focus on the monolayer and discuss the $3d$ orbital state (Sec. III A) and density of states (Sec. III B). Then we move to the magnetic properties of bilayer halides, by considering two different stacking arrangements. We concentrate on the interlayer exchange coupling, interpreting it in terms of virtual hopping mechanisms, highlighting the most efficient hopping paths (Sec. IV A) and addressing the effects of an external electric field in tuning the magnetic stability (Sec. IV B). Finally, we draw our conclusions in Sec. V.

II. COMPUTATIONAL METHOD

Density-functional theory (DFT) calculations were performed using the VASP code [23] within the generalized gradient approximation (GGA) [24]. The van der Waals (vdW) interactions were included for bilayer structure calculations. The rotationally invariant GGA+U method was employed to account for correlation effects [25]. On-site Coulomb interaction for transition-metal $3d$ orbitals was considered with an effective U of 2.0 eV [5,26]. We employed the experimental values for the in-plane lattice constants of both materials: For VI$_3$, we used $a = b = 6.84$ Å [15] and for CrI$_3$, we used $a = b = 6.87$ Å [8]. Details about binding energy calculations and the related determination of the interlayer d distance are reported in Supplemental Material [27]. A 20-Å-thick vacuum is contained in the supercell for 2D slab simulation. After the atomic structure was optimized using a k-point grid of $6 \times 6 \times 1$ until forces acting on atoms were smaller than 1×10^{-4} eV/Å, the SOC was included self-consistently. Density of states (also including electric fields) and total energy were calculated by using $12 \times 12 \times 1$ k-points mesh. Electric fields are applied perpendicularly to the surface by saw-tooth-like potential with dipole correction [28]. The maximally localized WANNIER functions (MLWFs) were calculated by using the WANNIER90 tool [29] interfaced with the VASP code.

III. RESULTS FOR MONOLAYER VI$_3$

A. $3d$-orbital state

First we focus on the difference between VI$_3$ and CrI$_3$ monolayers, as far as crystal-field effects are concerned. In particular, both VI$_3$ and CrI$_3$ are characterized by the magnetic cation coordinated to six I anions, forming edge-sharing octahedra and resulting in octahedral crystalline electric-field (CEF) splitting of the d orbitals into the twofold e_g and threefold t_{2g} states [see Figs. 1(a)–1(c)]. The t_{2g} state can be further split into a doublet e_g' and a singlet a_{1g} state under the trigonal crystal field in the honeycomb layer structure [18,30]. This effect may also couple to the trigonal lattice distortion when the t_{2g} orbitals are partially filled, but such Jahn-Teller distortion is not remarkable in this system. The I-Cr-I bond angle in CrI$_3$ is almost 90° (i.e., a cubic octahedron), while the I-V-I angle in VI$_3$ approaches 89°. Since the trigonal crystal-field effect is not strong enough to open the observed band gap in VI$_3$, we introduced the Hubbard U correction so as to
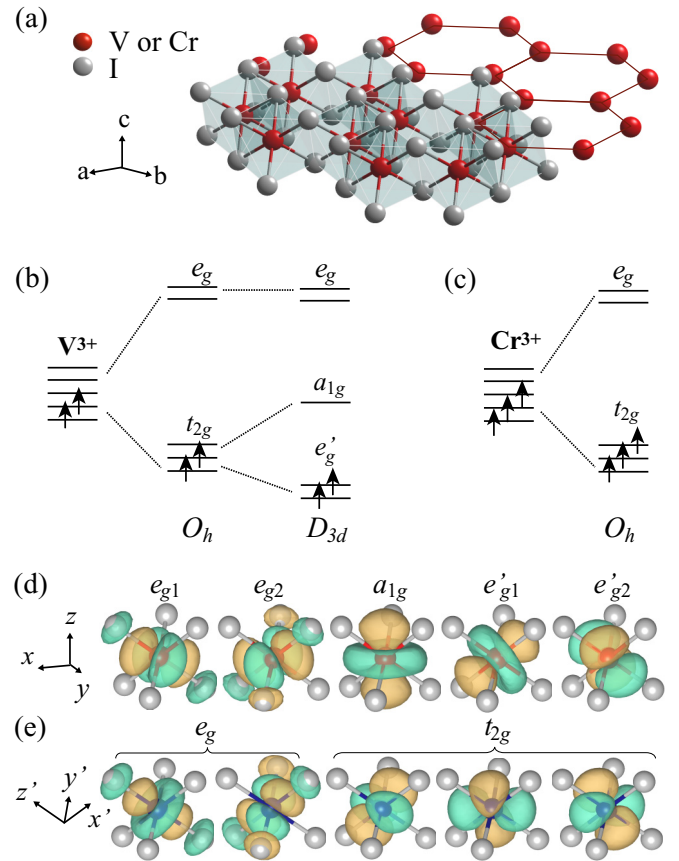

FIG. 1. (a) VI$_6$ (CrI$_6$) edge-sharing octahedra in the honeycomb layer structure. (b) and (c) The orbital splitting of d levels in V $3d^2$ and Cr $3d^3$, respectively. Five $3d$ WANNIER functions reflect the D_{3d} orbital basis set in monolayer VI$_3$ (d) and the O_h orbital basis set in monolayer CrI$_3$ (e). The isosurface levels of the WANNIER functions were set at $1.5 \, a_0^{-3/2}$ (yellow) and $-1.5 \, a_0^{-3/2}$ (blue), where a_0 is the Bohr radius.

split the t_{2g} orbital levels and obtain the insulating phase (see Supplemental Material for this paper [27] and that of Ref. [31] for the technical detail). Figures 1(b) and 1(c) show the difference in orbital splitting for VI$_3$ and CrI$_3$, respectively: As schematically represented, the t_{2g} orbital splitting allows for the band gap opening in VI$_3$ by half-filling the majority e_g' channel and leaving the a_{1g} empty in the case of V d^2. On the other hand, degeneracy of the t_{2g} orbital state is unlifted in the case of Cr d^3. The difference originates from the different occupation numbers and the Mott insulator nature that shifts up (down) the unoccupied (occupied) orbital levels by approximately a half amount of U value.

Therefore, the on-site Coulomb repulsion drives the t_{2g} orbital splitting in VI$_3$ and makes its orbital state distinct from that of CrI$_3$.

Within the global Cartesian $\{xyz\}$ coordinate system, Fig. 1(e), the a_{1g} and e_g' states are written in the form [32],

$$|a_{1g}\rangle = 3z^2 - r^2, \quad |e_{g1}'\rangle = \frac{1}{\sqrt{3}}(\sqrt{2}(x^2 - y^2) - zx),$$

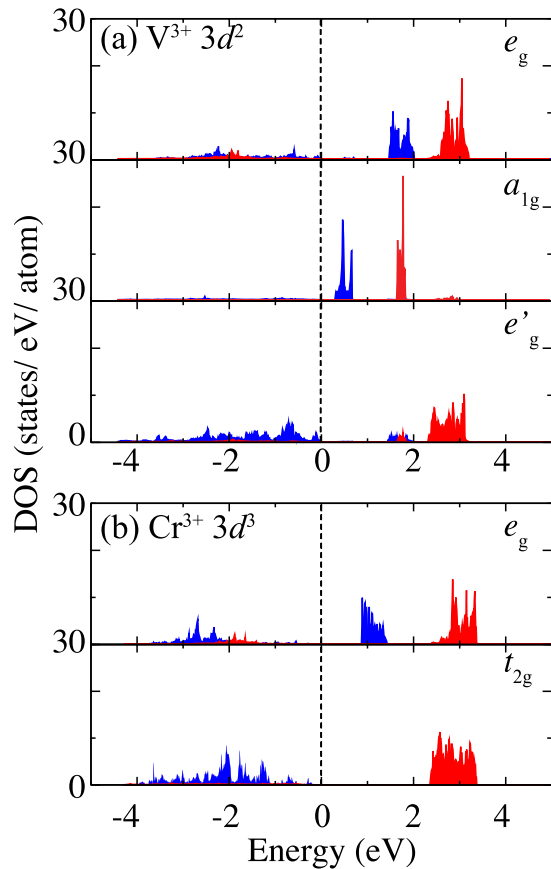$$|e_{g2}'\rangle = \frac{1}{\sqrt{3}}(\sqrt{2}xy + yz), \tag{1}$$

FIG. 2. The partial DOS (within $U = 2.0$ eV) projected onto (a) V-$3d$-D_{3d} and (b) Cr-$3d$-O_h orbital basis set, respectively, via WANNIER functions. Blue (red) color represents for majority spin (minority spin). The Fermi level is set as the energy origin.
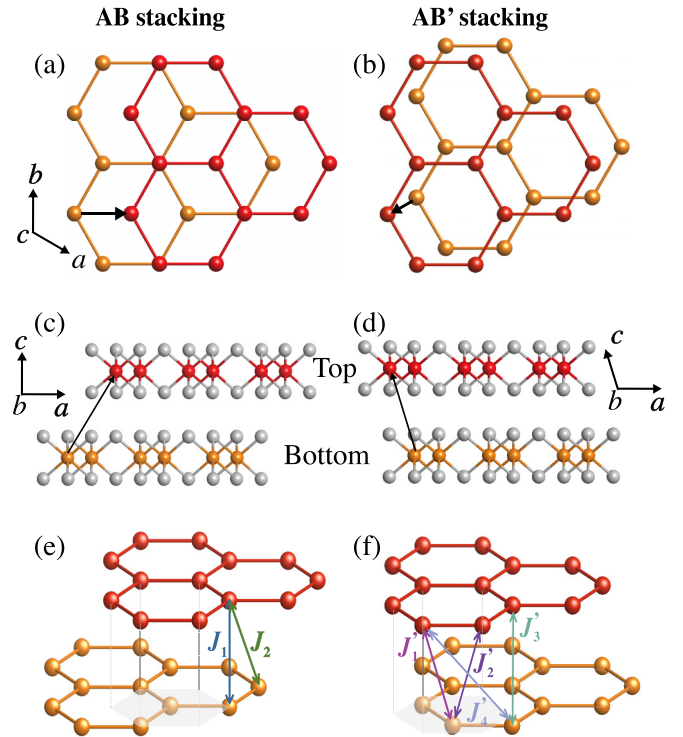

FIG. 3. (a) and (b) Top views and (c) and (d) side views of atomic structure in bilayer VI$_3$ in AB and AB′ stacking. The red and orange hexagons represent honeycomb structure of V atoms in top and bottom layers, and gray balls represent I atoms. The black arrow indicates the vector which connects equivalent atoms located in two layers and shows how the top layer is sliding with respect to the bottom layer. Interlayer exchange coupling J_{ij} in bilayer VI$_3$ for (e) AB and (f) AB′ stacking.

where the z axis is parallel to the out-of-layer direction (i.e., perpendicular to the slab). According to the different electron occupation and related orbital ground states, we projected the Bloch functions onto the local MI_6 octahedral coordinate system $\{x'y'z'\}$ for CrI$_3$ (with basis axes directed along the Cr-I bonds), and onto the Cartesian $\{xyz\}$ system for VI$_3$ [see Figs. 1(d) and 1(e) and Supplemental Material [27] for further technical details about WANNIER projection].

After the projection and maximally localization process, the WANNIER functions converged into localized orbitals, as shown in Figs. 1(d) and 1(e): orbital shapes are in agreement with the e_g-(a_{1g}, e'_g) states in VI$_3$ and the e_g-t_{2g} states in CrI$_3$. In particular, for the latter, it is possible to recognize the $|3z^2 - r^2\rangle$ orbital shape for the a_{1g} state (occupying the empty space at the center of the I$_3$ triangle and pointing along the z direction) and mixed shapes from the ($|x^2 - y^2\rangle$, $|zx\rangle$) and ($|xy\rangle$, $|yz\rangle$) orbitals for the e'_{g1} and e'_{g2} states, respectively, according to Eq. (1).

B. Density of states

In line with previous works, our DFT calculations on monolayer VI$_3$ converged to two different electronic states, corresponding to half-metallic [17] and Mott-insulator states [16,18]: The two V d^2 electrons occupy t_{2g} states as $a_{1g}^1 e_g'^1$ and $e_g'^2 a_{1g}^0$, respectively. We found that the insulating state (with a direct band gap of $\sim$0.39 eV at the Γ point for $U = 2.0$ eV) is lower in energy than the half-metallic state by 1.8 eV/f.u. Therefore, we will focus hereafter on the Mott insulator state as the ground state. As Yang *et al.* proposed that the insulating ground state of monolayer VI$_3$ is stabilized by spin-orbit coupling (SOC) splitting; the SOC effect originating from the heavy I elements is not negligible in VI$_3$ while the SOC effect does not play an important role in the usual 3d transition-metal compounds [33,34]. In fact, when including SOC in our band structure calculations, we observed that it affects the width and energy bands related to the I-p states, but it does not significantly change the V 3d band structure, as further argued in the Supplemental Material [27]. Moreover, as we focus here on the $e_g'^2 a_{1g}^0$ state, eventual SOC induced splitting would not affect the mechanisms and conclusions presented in this study.

The partial density of states (DOS) for monolayer CrI$_3$ and VI$_3$ are shown in Figs. 2(a) and 2(b), respectively; DOS are resolved for each MLWF state, clearly showing the e_g-a_{1g}-e_g' and e_g-t_{2g} orbital splitting for VI$_3$ and CrI$_3$, respectively, therefore validating our basis functions choice for the WANNIER projection as explained in the following.

TABLE I. Relative total energy (meV/f.u) for interlayer FM and AFM spin configurations in bilayers VI_3 and CrI_3 in AB and AB′ stacking. The lowest energy state is highlighted.

		AB	AB′
VI_3	FM	**0**	2.44
	AFM	0.69	**2.40**
CrI_3	FM	**0**	34.8
	AFM	14.7	36.6

We note that the Cr d^3 partial DOS, projected on the trigonal D_{3d} basic set (cf. Fig. 6 of Supplemental Material [27]), so as to allow a direct comparison with the V d^2 case, shows an overlap in the energy range of the a_{1g} and e'_g; this reflects the absence of splitting related to the Cr d^3 valence. In particular, Cr-d orbital states are split into empty e_g and occupied t_{2g} states with a gap of about 0.9 eV in the majority spin channel (up-spin states); the minority spin channel (down-spin states), unoccupied for both orbital types, does not display any relevant splitting. Such a different behavior between the majority and minority spin channels can be ascribed to the pd hybridization: the up-spin d states strongly hybridize with I-p states located at the top of the valence band, causing the large CEF splitting supported by the e_g-p bonding-antibonding splitting; the down-spin d states are higher in energy, i.e., away from I-p levels, thus not showing any significant CEF splitting.

In VI_3, the spin-up channel of the V d states are clearly split into e_g, a_{1g}, e'_g orbital states. In particular, the e'_g is the lowest energy state with a broad distribution due to the pd hybridization below the Fermi level, similar to the occupied t_{2g} state in CrI_3. At variance, the V-t_{2g} orbital splitting shows a different behavior of the empty d states: The a_{1g} state becomes the lowest energy state, while the e'_g state still lies in the same energy region as the minority Cr-t_{2g} state. This is consistent with the above-mentioned mechanism; the on-site Coulomb interaction opens an energy gap of the order of U between the occupied and unoccupied states. The different orbital-level alignment can be explained by the hybridization; the e'_g state has more bonding character with surrounding I p state than the a_{1g} state [compare the orbital shapes in Fig. 1(d)]; therefore, the pd hybridization shifts unoccupied e'_g level up and occupied I-p level down.

IV. RESULTS FOR BILAYER VI_3

A. Electronic properties and interlayer magnetic stability

Let us now consider the case of bilayer VI_3, showing a similar atomic structure to its bulk counterpart. In particular, we studied two structures corresponding to $R\bar{3}$ and $C2/c$ phases in bulk VI_3 [15]. The difference between these two structures is related to the different stacking of the two VI_3 single layers. As shown in Figs. 3(a) and 3(c), the AB stacking is characterized by the top layer showing one V atom sitting above the hexagon center of the bottom layer, similar to bilayer graphene. Indeed, when comparing equivalent atoms in two layers, the top layer is horizontally shifted from the bottom layers by $(2\boldsymbol{a} + \boldsymbol{b})/3$ (shown by a black arrow), where $\boldsymbol{a}$ and $\boldsymbol{b}$ denote the lattice vectors. This structure has $R\bar{3}$ symmetry. On the other hand, the AB′ stacking, with $C2/m$ space-group symmetry, is characterized by the shift of the top layer by $-(\boldsymbol{a} + \boldsymbol{b})/2$, as shown in Figs. 3(b) and 3(d).

First, we remark that the robustness of the intralayer FM spin ordering is demonstrated by calculating the energy difference between FM- and Néel-type antiferromagnetic AFM spin configurations in the VI_3 monolayer, i.e., $\Delta E = E_{AFM} - E_{FM} = 12.8$ meV/f.u. The V magnetic moment was calculated as 2.16 μ_B. We then address the magnetic properties of bilayers, by calculating the total energy between interlayer FM and AFM orders for the two stackings in bilayer VI_3 and compare the results with those obtained in CrI_3. In bilayer VI_3, the interlayer FM and AFM spin configurations are very close in energy; nevertheless, the FM order is favored in the AB stacking, while the AFM order is favored in AB′ stacking, as reported in Table I. Differently, in bilayer CrI_3, the FM order is favored in both AB and AB′ stacking patterns. Noteworthy, the interlayer FM order in AB′ stacking is only slightly more stable than the AFM order, the energy differences being rather sensitive to used on-site Coulomb U values, therefore not allowing a direct comparison with previous works on bilayer CrI_3. In any case, according to the energy differences reported in Table I, the magnetic stability in bilayers VI_3 and in CrI_3 AB′-stacking results to be weak. As such, it may lead to an easy control of the magnetism by either external electric fields or electrostatic doping.

To understand the magnetic stability, we evaluated the magnetic exchange interactions between V atoms by fitting total energies calculated in AB and AB′ stacking to the Heisenberg Hamiltonian. Here we assume the Heisenberg

TABLE II. Number of equivalent bonds per unit cell N, bond distance between transition-metal sites d, and calculated exchange coupling constants J_{ij} in AB and AB′ stacking for bilayers VI_3 and CrI_3.

		AB stacking			AB′ stacking				
		$J_\parallel$	J_1	J_2	$J_\parallel$	J'_1	J'_2	J'_3	J'_4
VI_3	N	6	1	9	6	2	2	2	2
	d (Å)	3.95	6.66	7.74	3.95	7.04	7.05	8.07	8.95
	J_{ij} (meV)	−3.20	0.81	−0.24	−4.46	0.10	0.21	0.04	−0.04
CrI_3	N	6	1	9	6	2	2	2	2
	d (Å)	3.95	6.57	7.68	3.95	7.00	7.02	8.03	8.92
	J_{ij} (meV)	−7.03	−0.82	−0.69	−8.11	−0.18	−0.23	−0.29	0.25

AB stacking | **AB' stacking**

VI₃ (a) 1ˢᵗ neighbor (b) 2ⁿᵈ neighbor | (c) 1ˢᵗ neighbor

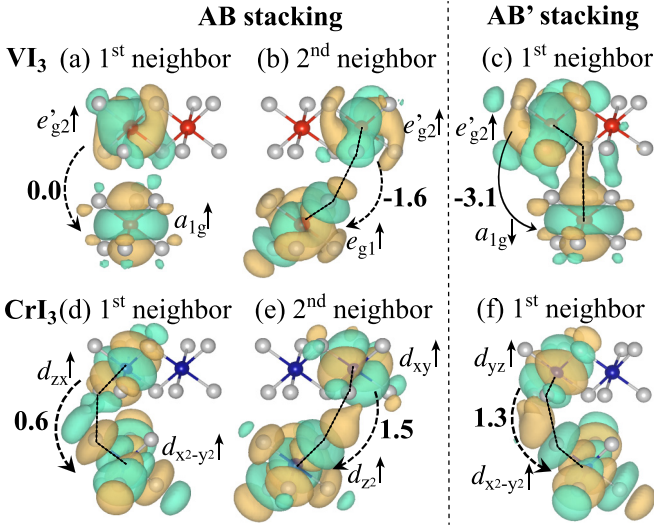**CrI₃**(d) 1ˢᵗ neighbor (e) 2ⁿᵈ neighbor | (f) 1ˢᵗ neighbor

FIG. 4. MLWFs relevant to interlayer exchange coupling in bilayers (a)–(c) VI_3 and (d)–(f) CrI_3. $\uparrow$ and $\downarrow$ denote the majority and minority spin states, respectively. The arrows show the electron hopping from an occupied orbital to an unoccupied orbital state; the dashed and solid lines denote the parallel-spin and anti-parallel-spin configurations, respectively. Values of the hopping integrals (meV) are also shown near the arrows. Isosurface levels were set at $\pm 0.45 \, a_0^{-3/2}$ for (a)–(c) and $\pm 0.3 \, a_0^{-3/2}$ for (d)–(f).

Hamiltonian,

$$H = \sum_{\langle i,j \rangle} J_{ij} \mathbf{s}_i \cdot \mathbf{s}_j, \tag{2}$$

where J_{ij} are the isotropic Heisenberg coupling constants between spin sites i and j and $\mathbf{s}_i$ is the unit vector pointing to the direction of the spin at site i. A parallel spin (FM) configuration is favored when $J < 0$ and an antiparallel (AFM) spin configuration is favored when $J > 0$.

In addition to the intralayer (in-plane) first nearest-neighbor coupling ($J_\parallel$), we thus considered interlayer couplings (J_1 and J_2 in AB stacking; J_1', J_2', J_3', and J_4' in AB' stacking) as schematically illustrated in Figs. 3(e) and 3(f); associated atomic pair distances are reported in Table II. In particular, we performed calculations to estimate J_2', J_3', and J_4' in a $2 \times 1 \times 1$ supercell via the four-state energy mapping method [35–39]. This method allows one to consider one specific pair of spins and remove the background interactions, therefore allowing the calculation of the interlayer magnetic exchange coupling constants of interest.

In Table II we report the estimated exchange coupling constants for bilayers VI_3 and CrI_3.

For VI_3, the intralayer exchange coupling favors the parallel spin state, while the interlayer coupling eventually favors the parallel spin state in AB stacking and antiparallel spin states in AB' stacking (cf. Table I). In closer detail, in AB stacking, J_1 favors antiparallel coupling (0.81 meV), while J_2 favors parallel coupling (−0.24 meV). Since there is one J_1 bond and nine J_2 bonds per unit cell, overall the ferromagnetic configuration is more stable. In AB' stacking, both J_1' and J_2' favor antiparallel coupling (0.1 meV and 0.21 meV), thus dominantly contributing to the interlayer AFM coupling stability. For CrI_3, the intralayer and interlayer exchange coupling basically favor parallel spin states in both AB stacking and AB' stacking.

In order to shed light on the microscopic mechanism behind the stacking-dependent magnetic couplings, we recall the *"virtual hopping"* idea based on the Hubbard model [32]. In particular, we discuss the results in terms of the virtual interlayer hopping of e_g-t_{2g} states supported by the interlayer M-I-I-M super-exchange effect. In the weak hopping limit, the intersite hopping can be treated as a perturbation to the ground state in which magnetic ordering does not affect the energy. When the hopping process is allowed between occupied and unoccupied states, it in turn contributes to the ground-state energy through the second-order contribution as the effective exchange energy $J_{\text{eff}} = 2t^2/U$ with hopping integral t and Coulomb repulsion U, the process being called "virtual

TABLE III. Hopping integrals calculated by MLWF basis set between occupied and unoccupied d orbital states in parallel ($t_{\uparrow\uparrow}$) or antiparallel ($t_{\uparrow\downarrow}$) spin configurations. Three types of hopping integrals, t_1, t_2, and t_1', corresponding with interlayer exchange couplings J_1, J_2, and J_1' are listed. $\Delta\varepsilon$ labels the difference between two eigenenergies for the MLWFs relevant to the hopping process, corresponding to $\Delta\varepsilon_{\uparrow\uparrow}$ and $\Delta\varepsilon_{\uparrow\downarrow}$ in the main text. The dominant hopping values relevant to the exchange couplings and those illustrated in Fig. 4 are highlighted in bold.

VI₃	Hopping $t_{\uparrow\uparrow}$				Hopping $t_{\uparrow\downarrow}$				
	$a_{1g}{}^0$-$a_{1g}{}^0$	$e_g{}^0$-$e_g{}^0$	$e_g'{}^2$-$a_{1g}{}^0$	$e_g'{}^2$-$e_g{}^0$	$a_{1g}{}^0$-$a_{1g}{}^0$	$e_g{}^0$-$e_g{}^0$	$e_g'{}^2$-$a_{1g}{}^0$	$e_g'{}^2$-$e_g{}^0$	$e_g'{}^2$-$e_g'{}^0$
$\Delta\varepsilon$ (eV)	0	0	1.4	1.5	1.4	2.1	2.9	3.4	3.5
t_1 (meV)	−3.6	2.1	**0.0**	−0.7	−4.6	2.7	0.0	1.0	0.6
t_2 (meV)	−0.7	1.1	0.3	**−1.6**	−0.5	−0.9	−0.6	2.6	−1.0
t_1' (meV)	3.6	1.0	−1.1	1.6	4.9	1.1	**−3.1**	3.1	−3.3

CrI₃	Hopping $t_{\uparrow\uparrow}$			Hopping $t_{\uparrow\downarrow}$		
	$e_g{}^0$-$e_g{}^0$	$t_{2g}{}^3$-$e_g{}^0$	$t_{2g}{}^3$-$t_{2g}{}^3$	$e_g{}^0$-$e_g{}^0$	$t_{2g}{}^3$-$e_g{}^0$	$t_{2g}{}^3$-$t_{2g}{}^3$
$\Delta\varepsilon$ (eV)	0	1.5	0	2.7	4.3	4.6
t_1 (meV)	0.9	**0.6**	0.7	1.3	−1.1	1.7
t_2 (meV)	0.6	**1.5**	0.8	0.6	2.7	−1.3
t_1' (meV)	2.1	**1.3**	1.4	3.0	−3.1	4.6

hopping." If we consider the direct hopping between occupied and unoccupied $3d$ states at the transition metal sites, the parallel-spin configuration is favored if the hopping is strong between majority- and majority-spin states; on the other hand, the antiparallel spin configuration is favored if the hopping between majority- and minority-spin states is strong. In order to discuss the virtual hopping process, we extracted the hopping parameters by using a MLWF basis set, as illustrated in Figs. 1(e) and 1(f). Note that the WANNIER functions are centered at V and Cr sites and spreading the tail to I sites, so that our virtual hopping process implicitly includes the pd hybridization process. The same concept can be found in Anderson's original work on super-exchange interaction [40].

Figure 4 shows the interlayer hopping paths with the corresponding MLWFs which are responsible for the exchange energy in bilayers VI_3 and CrI_3. Here we select three types of interlayer exchange couplings: first-neighbor and second-neighbor (J_1 and J_2) interactions in AB stacking; first-neighbor (J_1') interaction in AB' stacking. The calculated hopping integrals corresponding to these exchange couplings are shown in Table III.

In AB-stacking bilayer VI_3, the trigonal CEF levels and the two-electron occupation make J_1 positive (antiparallel-spin-favored). The hopping between $e_{g2}'^\uparrow$ and $a_{1g}^\uparrow$ states are calculated to be negligible ($t \sim 0.0$ meV), thus not contributing to the magnetic interaction. On the other hand, the hopping between $e_{g2}'^\uparrow$ and $e_g^\downarrow$ states is sizable ($t=1.0$ meV), which may be responsible for the antiparallel-spin-favored exchange interaction. In the AB-stacking bilayer CrI_3, in contrast, the negative (parallel-spin-favored) J_1 can be explained by a sizable hopping between the occupied $d_{zx}^\uparrow$ state and the unoccupied $d_{x^2-y^2}^\uparrow$ state ($t=0.6$ meV). This is consistent with previous works, claiming that the e_g-t_{2g} hopping leads to the FM coupling [9,41]. As shown in Fig. 4(d), the diagonally elongated lobes of d_{zx} and $d_{x^2-y^2}$ orbitals show a path through Cr-I-I-Cr sites with $d_{zx}^\uparrow$-p–p-$d_{x^2-y^2}^\uparrow$ hybridization, where the first pd hybridization shows π-like and the second shows σ-like bonding. The second neighbor interaction J_2 is negative both for VI_3 and CrI_3. This can be explained by a large hopping integral between $e_{g2}'^\uparrow$ and $e_{g1}^\uparrow$ and that between $d_{xy}^\uparrow$ and $d_{z^2}^\uparrow$ states. In Fig. 4(b), we can recognize a $e_{g2}'^\uparrow$-p-$e_{g1}^\uparrow$ hybridization, where the pd hybridization shows σ bonding. For the CrI_3 case, a similar picture holds [cf. Fig. 4(e)], where the e_{g2}' orbital is replaced by the d_{xy} orbital.

The AB'-stacked bilayer VI_3 shows an interesting interplay between the atomic arrangement and the specific character of the a_{1g} orbital of V, related to the VI_3 orbital splitting: Since a vanadium atom in the bottom layer is located right under an iodine atom in the upper layer, the V-a_{1g} orbital strongly overlaps with the I-p_z orbital and forms the σ bonding [Fig. 4(c)]. This makes the e_{g2}'-a_{1g} hopping relevant; in particular, the $e_{g2}'^\uparrow$-p–$a_{1g}^\downarrow$ hopping is very strong ($t = -3.1$ meV), making J_1' positive. In AB' stacked bilayers, the interlayer exchange interactions are weaker than those in AB stacked bilayers, since several possible hoppings between multiple orbital states tend to cancel each other due to the atomic arrangement. In evident contrast, the AB'-stacked bilayer CrI_3 shows results similar to the AB-stacked case: The $d_{yz}^\uparrow$-p-p-$d_{x^2-y^2}^\uparrow$ hybridization path,
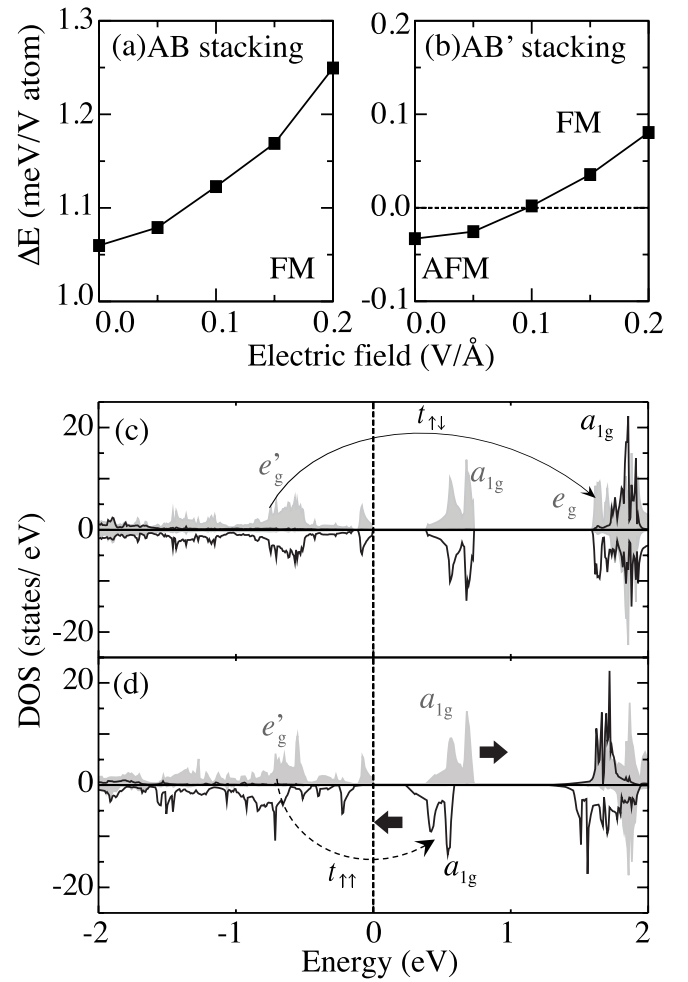

FIG. 5. The energy difference between the FM and AFM ordering for (a) AB and (b) AB' stacking as a function of an external electric field. The positive value of ΔE means FM is favored and negative means AMF is favored. d-orbital projected density of state for top (solid filled) and bottom (solid line) layer of bilayer VI_3 with AFM AB' stacking in AFM ordering (c) without and (d) with external electric field. Black arrow presents for the energy shifted by applied electric field. Vertical dash line denotes the Fermi energy.

where the former (latter) pd hybridization shows π (σ) bonding, makes J_1' negative [Fig. 4(f)].

B. Electric-field control of magnetic stability

Finally, we discuss the effect of an applied electric field on the magnetic stability in bilayer VI_3. This is indeed relevant, since a magnetic phase transition upon electric-field application has been reported in bilayer CrI_3 [4–6]. The energy difference between interlayer AFM and FM states in AB and AB' stacked with applied electric fields is shown in Fig. 5. In both stacking cases, an applied electric field promotes the FM ordering. Remarkably, in the AB' stacking, the ground state switches from AFM to FM ordering when the electric fields exceed a threshold value of ~ 0.1 V/Å.

The microscopic mechanism of the tunable magnetic stability can be explained by invoking again the virtual hopping idea. The DOS projected onto the V-d orbital state of top

and bottom layers in AB′ stacked bilayer VI_3 is shown in Figs. 5(c) and 5(d). Without electric field, the DOS relative to the top and bottom layers lie in the same energy range. As discussed above, there is a competition between parallel-spin hopping and antiparallel-spin hopping in determining the first-neighbor exchange coupling J_1'. Since the energy difference between the $e_g'^{\uparrow}$ and $a_{1g}^{\downarrow}$ states ($\Delta\varepsilon_{\uparrow\downarrow} = 2.9$ eV) is much larger than the energy difference between the $e_g'^{\uparrow}$ and $a_{1g}^{\uparrow}$ states ($\Delta\varepsilon_{\uparrow\uparrow} = 1.4$ eV), one may think that a parallel-spin configuration is favored. However, J_1' is found to be slightly AFM favored. This is because the antiparallel-spin hopping ($t_{\uparrow\downarrow} = -3.1$ meV) is stronger than the parallel-spin hopping ($t_{\uparrow\uparrow} = -1.1$ meV), resulting in a stronger AFM effective exchange coupling $J_{\text{eff}} \propto t^2/\Delta\varepsilon$. Upon electric fields, the a_{1g} orbital state of the top layer is shifted up, while it is shifted down in the bottom layer (cf. Fig. 5). The band gap becomes narrower due to the shift of DOS and in turn the difference between orbital energy levels decreases, while the hopping integral is not significantly affected. Overall, this increases the tendency toward FM stability, eventually switching the favored magnetic configuration from AFM to FM.

V. CONCLUSIONS

By means of first-principles calculations, we investigated the magnetic stability in bilayer VI_3 and compared our results with the corresponding well-studied case of CrI_3. In particular, the magnetic exchange interactions have been analyzed by evaluating the hopping integrals between MLWFs projected onto $3d$ orbital states at V and Cr sites. We found out that the trigonal crystal-field orbital splitting enhanced by the on-site Coulomb repulsion U within a single layer of VI_3 plays an important role for the interlayer magnetic exchange interaction. The t_{2g} orbital states are in fact split into e_g' and a_{1g} states; the latter shows the typical lobe shape pointing along the out-of-plane direction and the strong hopping between bottom-layer a_{1g} and top-layer e_g' states determine the antiferromagnetic interlayer coupling in the AB′ stacking bilayer VI_3. Nevertheless, since the hoppings favoring parallel-spin and antiparallel-spin configurations are highly competing, the application of electric fields allows the switching of the interlayer magnetic ordering from AFM to FM, paving the way to spintronic applications of VI_3-based 2D magnets.

[1] B. Huang, G. Clark, E. Navarro-Moratalla, D. R. Klein, R. Cheng, K. L. Seyler, D. Zhong, E. Schmidgall, M. A. McGuire, D. H. Cobden, W. Yao, D. Xiao, P. Jarillo-Herrero, and X. Xu, Nature (London) **546**, 270 (2017).

[2] C. Gong, L. Li, Z. Li, H. Ji, A. Stern, Y. Xia, T. Cao, W. Bao, C. Wang, Y. Wang, Z. Q. Qiu, R. J. Cava, S. G. Louie, J. Xia, and X. Zhang, Nature (London) **546**, 265 (2017).

[3] Y. Deng, Y. Yu, Y. Song, J. Zhang, N. Z. Wang, Z. Sun, Y. Yi, Y. Z. Wu, S. Wu, J. Zhu, J. Wang, X. H. Chen, and Y. Zhang, Nature (London) **563**, 94 (2018).

[4] B. Huang, G. Clark, D. R. Klein, D. MacNeill, E. Navarro-Moratalla, K. L. Seyler, N. Wilson, M. A. McGuire, D. H. Cobden, D. Xiao, W. Yao, P. Jarillo-Herrero, and X. Xu, Nat. Nanotechnol. **13**, 544 (2018).

[5] S. Jiang, J. Shan, and K. F. Mak, Nat. Mater. **17**, 406 (2018).

[6] E. S. Morell, A. León, R. H. Miwa, and P. Vargas, 2D Materials **6**, 025020 (2019).

[7] S. Jiang, L. Li, Z. Wang, K. F. Mak, and J. Shan, Nat. Nanotechnol. **13**, 549 (2018).

[8] M. A. McGuire, H. Dixit, V. R. Cooper, and B. C. Sales, Chem. Mater. **27**, 612 (2015).

[9] N. Sivadas, S. Okamoto, X. Xu, C. J. Fennie, and D. Xiao, Nano Lett. **18**, 7658 (2018).

[10] D. Soriano, C. Cardoso, and J. Fernández-Rossier, Solid State Commun. **299**, 113662 (2019).

[11] P. Jiang, C. Wang, D. Chen, Z. Zhong, Z. Yuan, Z.-Y. Lu, and W. Ji, Phys. Rev. B **99**, 144401 (2019).

[12] J. Kim, K.-W. Kim, B. Kim, C.-J. Kang, D. Shin, S.-H. Lee, B.-C. Min, and N. Park, Nano Lett. **20**, 929 (2020).

[13] D.-H. Kim, K. Kim, K.-T. Ko, J. H. Seo, J. S. Kim, T.-H. Jang, Y. Kim, J.-Y. Kim, S.-W. Cheong, and J.-H. Park, Phys. Rev. Lett. **122**, 207201 (2019).

[14] S. Son, M. J. Coak, N. Lee, J. Kim, T. Y. Kim, H. Hamidov, H. Cho, C. Liu, D. M. Jarvis, P. A. C. Brown, J. H. Kim, C.-H. Park, D. I. Khomskii, S. S. Saxena, and J.-G. Park, Phys. Rev. B **99**, 041402(R) (2019).

[15] S. Tian, J.-F. Zhang, C. Li, T. Ying, S. Li, X. Zhang, K. Liu, and H. Lei, J. Am. Chem. Soc. **141**, 5326 (2019).

[16] Y.-P. Wang and M.-Q. Long, Phys. Rev. B **101**, 024411 (2020).

[17] C. Huang, F. Wu, S. Yu, P. Jena, and E. Kan, Phys. Chem. Chem. Phys. **22**, 512 (2020).

[18] K. Yang, F. Fan, H. Wang, D. I. Khomskii, and H. Wu, Phys. Rev. B **101**, 100402(R) (2020).

[19] J. He, S. Ma, P. Lyu, and P. Nachtigall, J. Mater. Chem. C **4**, 2518 (2016).

[20] T. Kong, K. Stolze, E. I. Timmons, J. Tao, D. Ni, S. Guo, Z. Yang, R. Prozorov, and R. J. Cava, Adv. Mater. **31**, 1808074 (2019).

[21] J. A. Wilson, C. Maule, P. Strange, and J. N. Tothill, J. Phys. C **20**, 4159 (1987).

[22] C. Long, T. Wang, H. Jin, H. Wang, and Y. Dai, J. Phys. Chem. Lett. **11**, 2158 (2020).

[23] G. Kresse and J. Furthmüller, Phys. Rev. B **54**, 11169 (1996).

[24] J. P. Perdew, K. Burke, and M. Ernzerhof, Phys. Rev. Lett. **77**, 3865 (1996).

[25] S. L. Dudarev, G. A. Botton, S. Y. Savrasov, C. J. Humphreys, and A. P. Sutton, Phys. Rev. B **57**, 1505 (1998).

[26] A. I. Liechtenstein, V. I. Anisimov, and J. Zaanen, Phys. Rev. B **52**, R5467 (1995).

[27] See Supplemental Material at http://link.aps.org/supplemental/10.1103/PhysRevB.104.014414 for detailed calculations.

[28] J. Neugebauer and M. Scheffler, Phys. Rev. B **46**, 16067 (1992).

[29] A. A. Mostofi, J. R. Yates, Y.-S. Lee, I. Souza, D. Vanderbilt, and N. Marzari, Comput. Phys. Commun. **178**, 685 (2008).

[30] W. B. Wu, D. J. Huang, J. Okamoto, A. Tanaka, H.-J. Lin, F. C. Chou, A. Fujimori, and C. T. Chen, Phys. Rev. Lett. **94**, 146402 (2005).

[31] K. Yamauchi and S. Picozzi, Phys. Rev. Lett. **105**, 107202 (2010).

[32] D. I. Khomskii, *Transition Metal Compounds* (Cambridge University Press, Cambridge, 2014).

[33] J. B. Goodenough, Phys. Rev. **171**, 466 (1968).

[34] P. Bruno, Phys. Rev. B **39**, 865 (1989).

[35] H. J. Xiang, E. J. Kan, S.-H. Wei, M.-H. Whangbo, and X. G. Gong, Phys. Rev. B **84**, 224429 (2011).

[36] H. Xiang, C. Lee, H.-J. Koo, X. Gong, and M.-H. Whangbo, Dalton Trans. **42**, 823 (2013).

[37] D. Šabani, C. Bacaksiz, and M. V. Milošević, Phys. Rev. B **102**, 014457 (2020).

[38] C. Xu, J. Feng, S. Prokhorenko, Y. Nahas, H. Xiang, and L. Bellaiche, Phys. Rev. B **101**, 060404(R) (2020).

[39] C. Xu, J. Feng, H. Xiang, and L. Bellaiche, npj Comput. Mater. **4**, 57 (2018).

[40] P. W. Anderson, Phys. Rev. **115**, 2 (1959).

[41] S. W. Jang, M. Y. Jeong, H. Yoon, S. Ryee, and M. J. Han, Phys. Rev. Materials **3**, 031001(R) (2019).

[42] K. Momma and F. Izumi, J. Appl. Cryst. **44**, 1272 (2011).